ORIGINAL ARTICLE

Geological cycling of potassium and the K isotopic response: insights from loess and shales

Weiqiang Li[1] · Shilei Li[2] · Brian L. Beard[3,4]

Abstract Shales are a major sink for K into seawater delivered from continental weathering, and are potential recorders of K cycling. High precision K isotope analyses reveal a > 0.6 ‰ variation in $\delta^{41}K$ values ($^{41}K/^{39}K$ relative to NIST SRM 3141a) from a set of well characterized post-Archean Australian shale (PAAS) samples. By contrast, loess samples have relatively homogenous $\delta^{41}K$ values (-0.5 ± 0.1 ‰), which may represent the average K composition of upper continental crust. Most of the shales analyzed in this study have experienced K enrichment relative to average continental crust, and the majority of them define a trend of decreasing $\delta^{41}K$ value (from -0.5 to -0.7 ‰) with increasing K content and K/Na ratio, indicating cation exchange in clays minerals is accompanied by K isotope fractionation. Several shale samples do not follow the trend and have elevated $\delta^{41}K$ values up to -0.1 ‰, and these samples are characterized by variable Fe isotope compositions, which reflect post-depositional processes. The K isotope variability observed in shales, in combination with recent findings about K isotope fractionation during continental weathering, indicates that K isotopes fractionate during cycling of K between different reservoirs, and K isotopes in sediments may be used to trace geological cycling of K.

1 Introduction

Potassium (K) is a major constituent in Earth's mantle (190–260 ppm; Palme and O'Neill 2014), crust (2.3 wt%; Rudnick and Gao 2003), river waters (0.2–20 ppm; Meybeck 2003), and seawater (399 ppm). During its global cycling, K is added into oceans via riverine runoff and mid-ocean ridge (MOR) hydrothermal fluxes (Elderfield and Schultz 1996a; Garrels and Mackenzie 1971). The influx of K in seawater is balanced by K removal by chemical exchange involving clays in sediments, and low temperature basalt alteration (Bloch and Bischoff 1979; Kronberg 1985). The K influx is affected by the relative intensity of continental weathering and mid-ocean ridge activities. Changes in the relative intensity of continental weathering and MOR activities have been suggested to account for the changes in seawater chemistry, and the shifting between "calcite sea" and "aragonite sea" in the Phanerozoic (Hardie 1996). In addition, either changes in mid-ocean ridge spreading rate (Berner et al. 1983) or changes in erosion due to mountain uplift (Raymo and Ruddiman 1992) have been suggested to be the primary driving force for variations in atmospheric CO_2 level, a topic that has been hotly debated for decades. Understanding of the relative intensity of continental weathering and mid-ocean ridge activities from a perspective of K cycling, therefore, may provide insights into the fundamental questions about secular changes in ocean chemistry and sediment

✉ Weiqiang Li
  liweiqiang@nju.edu.cn

[1] State Key Laboratory for Mineral Deposits Research, School of Earth Sciences and Engineering, Nanjing University, Nanjing 210046, People's Republic of China

[2] MOE Key Laboratory of Surficial Geochemistry, School of Earth Sciences and Engineering, Nanjing University, Nanjing 210046, People's Republic of China

[3] Department of Geoscience, University of Wisconsin-Madison, 1215W Dayton Street, Madison, WI 53706, USA

[4] NASA Astrobiology Institute, University of Wisconsin–Madison, Madison, WI 53706, USA

mineralogy, as well as atmospheric CO_2 levels in geological history.

Potassium has three naturally occurring isotopes, which are ^{39}K (93.258%), ^{40}K (0.012%, radioactive, half-life 1.248 billion years), and ^{41}K (6.730%). The precisions of $^{41}K/^{39}K$ ratio measurements in earlier studies using TIMS and SIMS techniques were not sufficient to resolve the sub per mil level K isotope differences between most terrestrial samples (Humayun and Clayton 1995). Recently, advances in multi-collector inductively coupled plasma mass spectrometry (MC-ICP-MS) has led to significant improvements in precision of $^{41}K/^{39}K$ ratio measurements (Li et al. 2016; Morgan et al. 2018; Wang and Jacobsen2016). Indeed, the $^{41}K/^{39}K$ ratio can be can be routinely measured to a precision of better than 0.1 ‰ (Chen et al. 2019; Hu et al. 2018; Xu et al. 2019). Subsequently, significant K isotope fractionation effects have been observed during biological processes (Li 2017), K-salts precipitation (Li et al. 2017), and continental weathering (Li et al. 2019). One of the remarkable discoveries with the improved analytical precision is that modern seawater has a $^{41}K/^{39}K$ ratio that is about 0.6 ‰ higher than igneous rocks (Li et al. 2016; Wang and Jacobsen 2016). The cause of such isotopic contrast, however, is not known yet. Here we report new K isotope data for a range of well-characterized loess and shale samples to better understand the origin of the K isotope difference between seawater and igneous rocks, and to explore the potential of K isotope geochemistry for tracing global K cycling.

2 Materials and methods

2.1 Samples and preparation

Most of the shale and loess samples analyzed in this study were originally collected to characterize the composition of upper continental crust (Nance and Taylor 1976; Taylor et al. 1983). Specifically, the shale samples were used to define the post Archean Australian shale (PAAS) composite for rare earth element concentrations. All of the shale samples are from areas of unmetamorphosed regions extending back into the Proterozoic, and these samples are from deep drill cores and thus were not subject to surface weathering and leaching like samples from outcrops (Nance and Taylor 1976). Also analyzed were three USGS rock standards that included modern marine mud (MAG-1) and two shales (SCo-1 and SGR-1; Flanagan 1976). Loess samples analyzed in this study are from Germany, New Zealand and United States, which were originally collected and studied by Taylor et al. (1983). Detailed Fe isotope analyses by Beard et al. (2003) have been reported on these shale and loess samples, and these results are used to aid in

interpreting the K isotope data. Chemical and Fe isotope compositions of the loess and shale samples are provided in Table 1.

Sample preparation was undertaken at Nanjing University, where all chemical procedures were performed in a clean room (class 1000) with laminar flow hoods (class 100) and HEPA filtered air. Deionized (18.2 MΩ) water, Teflon-coated hot plates, Teflon beakers, double distilled reagents were used throughout the experiments; other labwares, such as centrifuge tubes and pipette tips, were soaked in 6 M HCl overnight and rinsed using deionized water before usage. Silicate powders were dissolved using a standard HF-HNO$_3$ digestion procedure at 130 °C. An aliquot of the dissolved sample, which typically contained 50–200 μg of K, was converted into nitrate salts by repeatedly drying and re-dissolution in 50–100 μL concentrated HNO_3. The sample was subsequently dried and dissolved in 0.5 mL 1.5 M HNO_3, and ready for chemical purification using ion exchange chromatography.

Separation of K from matrix elements followed a two-stage ion exchange protocol that has been described in Li et al. (2016). A dissolved sample was firstly loaded on to a first-stage column that contained 1 mL wet volume (in deionized water, gravity packing) of 100–200 mesh BioRad® AG50W-x12 resin and eluted using 1.5 M HNO_3. Effective separation of K from Na, Al and Ca was achieved using the first stage column, but a proportion of Ti and all of Mg was also collected with K. The K-bearing solution collected from the first stage column was dried and re-dissolved in a weak HNO_3-HF acid that contained 0.2 M HNO_3 and 0.05 M HF, and loaded onto the second stage column that contained 0.4 mL wet volume of 100–200 mesh BioRad® AG50 W-x8 resin, and was pre-conditioned with the weak HNO_3-HF acid. Ti^{4+} form ion-complex with F^- and was effectively washed off the cation exchange resin during elution with the weak HNO_3-HF acid. Following that, a 0.5 M HNO_3 was used to effectively separate K from Mg and the remaining vestiges of Na (Li et al. 2016). Such two-stage column procedure balances between versatility, quality of separation, robustness, acid consumption, and efficiency for chemical purification of K. Potassium recovery of the method was 99.4 ± 2.1 ‰ (2SD, n = 54), and the total procedural blank of K was 3–8 ng (n = 5), which is negligible compared with the > 50 μg mass of K in samples.

2.2 Mass spectrometry

$^{41}K/^{39}K$ isotope ratio measurements were performed on a Micromass IsoProbe MC-ICP-MS at the University of Wisconsin-Madison, using instrument settings that have been detailed in Li et al. (2016). The IsoProbe MC-ICP-MS was run with a standard 1350 W forward RF power, using high purity He (flow rate: 10 mL/min) as the collision gas

Table 1 K isotope composition, Fe isotope composition, and major element concentrations of loess and shale samples

Sample[a] Name	$\delta^{56}Fe^b$ ‰	1SD ‰	$\delta^{41}K^c$ ‰	2SD ‰	n	SiO$_2$ wt%	TiO$_2$ wt%	Al$_2$O$_3$ wt%	Fe$_2$O$_3$ wt%	MgO wt%	CaO wt%	Na$_2$O wt%	K$_2$O wt%	MnO wt%	P$_2$O$_5$ wt%	LOI wt%	Sum wt%
Kaierstuhl Loess																	
Ksthl-1	0.01	0.09	− 0.43	0.06	2	59.90	0.32	7.78	3.22	3.45	23.11	0.84	1.27	0.07			99.96
Ksthl-2	0.04	0.09	− 0.48	0.23	3	59.10	0.29	7.98	2.94	4.37	22.90	0.87	1.34	0.07			99.86
Loess Banks Peninsula																	
BP-1	0.02	0.08	− 0.57	0.05	2	72.70	0.57	15.80	3.30	0.95	1.54	3.27	2.39	0.05			100.57
BP-2	− 0.02	0.06	− 0.58	0.03	2	74.00	0.55	14.70	3.38	0.97	1.47	3.05	2.31	0.05			100.48
BP-3	0.05	0.05	− 0.57	0.03	2	72.50	0.69	15.20	3.94	0.88	1.27	3.13	2.26	0.05			99.93
BP-4			− 0.54	0.02	2	74.00	0.57	14.30	3.44	1.07	1.27	3.43	2.42	0.06			100.56
BP-5	0.12	0.05	− 0.54	0.01	2	72.50	0.54	15.10	3.21	1.06	1.58	3.55	2.47	0.05			100.06
Kansas-Iowa Loess																	
CY-4a-A	0.07	0.10	− 0.45	0.05	2	80.40	0.64	10.50	2.58	0.86	1.12	1.58	2.53	0.04			100.25
CY-4a-B	0.07	0.06	− 0.43	0.01	2	80.80	0.63	10.60	2.64	0.95	1.09	1.60	2.57	0.05			100.93
CY-4a-C	0.10	0.08	− 0.47	0.02	2	79.90	0.71	10.70	2.54	0.88	1.23	1.68	2.62	0.04			100.31
Iowa	− 0.08	0.10	− 0.46	0.20	2	79.50	0.69	11.40	3.01	1.01	0.85	1.45	2.18	0.00			100.09
Amadeus Basin Shale																	
AO6	0.03	0.02	− 0.34	0.15	2	61.13	0.65	14.54	5.80	3.48	2.45	0.93	4.34	0.12	0.06	6.24	99.74
AO7	− 0.28	0.10	− 0.61	0.12	2	61.75	0.72	14.50	7.81	2.60	1.22	0.80	4.24	0.12	0.05	6.66	100.47
AO8			− 0.66	0.11	2	70.00	0.71	13.20	5.31	1.52	0.32	0.93	3.34	0.02	0.10	4.71	100.16
AO9	− 0.01	0.10	− 0.64	0.02	2	65.83	0.72	14.57	6.79	2.29	0.40	0.98	3.66	0.11	0.08	4.81	100.24
AO10	0.10	0.04	− 0.65	0.12	2	62.97	0.80	15.84	7.08	1.92	0.25	0.94	4.16	0.08	0.11	5.57	99.72
AO12	0.39	0.07	− 0.08	0.10	2	56.56	0.79	20.66	5.75	3.13	0.13	0.82	8.41	0.02	0.05	3.86	100.18
Mt. Isa Group Shale																	
MI-1	0.15	0.06	− 0.38	0.17	4	70.97	0.45	13.84	4.20	2.46	0.34	1.13	3.60	0.04	0.21	3.38	100.62
MI12	− 0.01	0.05	− 0.35	0.13	2	56.15	0.26	6.91	2.05	4.92	12.06	3.38	0.75	0.35	0.14	13.90	100.87
MI14	0.09	0.04	− 0.55	0.08	2	69.80	0.49	13.33	3.98	1.48	0.80	1.70	2.88	0.06	0.18	5.70	100.40
MI15	− 0.02	0.10	− 0.44	0.10	2	65.86	0.75	14.70	6.51	2.46	0.48	0.40	3.69	0.04	0.30	4.29	99.48
Canning Basin Shale																	
PL-1	0.01	0.08	− 0.48	0.05	2	63.51	0.73	18.76	5.81	1.53	0.37	0.17	4.09	0.04	0.08	4.34	99.43
PL-6	0.00	0.07	− 0.59	0.01	2	61.08	0.68	15.67	4.93	1.86	4.73	0.43	3.47	0.05	0.10	7.31	100.31
Perth Basin Shale																	
PW4	− 0.01	0.04	− 0.56	0.01	2	57.86	0.99	22.46	7.89	1.80	0.40	0.90	3.99	0.08	0.19	4.05	100.61
PW-5	0.03	0.06	− 0.60	0.05	2	55.34	0.96	22.08	8.82	1.68	0.53	0.88	3.20	0.15	0.21	5.50	99.35
PW-7	0.21	0.00	− 0.60	0.14	2	59.56	0.91	19.17	10.41	1.99	0.53	1.68	2.69	0.11	0.15	3.58	100.78
State Circle Shale																	
SC1	− 0.04	0.10	− 0.63	0.06	2	65.07	0.70	16.34	6.55	2.77	0.24	0.46	4.01	0.41	0.14	3.20	99.89

Table 1 continued

Sample[a] Name	$\delta^{56}Fe$[b] ‰	1SD ‰	$\delta^{41}K$[c] ‰	2SD ‰	n	SiO$_2$ wt%	TiO$_2$ wt%	Al$_2$O$_3$ wt%	Fe$_2$O$_3$ wt%	MgO wt%	CaO wt%	Na$_2$O wt%	K$_2$O wt%	MnO wt%	P$_2$O$_5$ wt%	LOI wt%	Sum wt%
SC2	− 0.02	0.06	− 0.67	0.08	2	65.34	0.71	16.50	6.25	2.63	0.23	0.36	4.23	0.25	0.15	3.18	99.83
SC3			− 0.65	0.03	2	67.03	0.68	15.32	6.51	2.67	0.22	0.45	3.69	0.39	0.15	3.09	100.20
SC4	− 0.04	0.04	− 0.63	0.11	2	64.65	0.70	16.52	6.52	2.81	0.24	0.30	4.16	0.40	0.16	3.28	99.74
SC5	0.02	0.07	− 0.69	0.07	2	65.34	0.72	17.00	5.99	2.68	0.22	0.25	4.45	0.25	0.15	3.26	100.31
SC7	0.01	0.09	− 0.68	0.06	2	65.58	0.69	16.16	7.17	2.80	0.23	0.37	3.85	0.20	0.14	3.22	100.41
SC8			− 0.64	0.04	2	65.58	0.72	16.51	6.32	2.63	0.21	0.64	4.09	0.22	0.14	3.12	100.18
Green River shale																	
SGR-1	− 0.34	0.15	− 0.36	0.19	3	28.29	0.35	7.24	3.20	4.50	8.87	2.66	1.71	0.04	0.29		
Modern marine mud																	
MAG-1	− 0.04	0.07	− 0.57	0.06	2	50.87	0.75	16.77	7.09	2.83	1.41	3.43	3.57	0.11	0.17		
Cody shale																	
SCO-1			− 0.41	0.17	4	61.84	0.83	13.40	3.83	2.69	2.68	0.97	2.80	0.05	0.44		
Upper continental crust	0.00					66.62	0.64	15.40	5.04	2.48	3.59	3.27	2.80	0.10	0.15		

[a] Description and elemental data of loess and shales samples are from Taylor et al. (1983) and Nance and Taylor (1976)

[b] Fe isotope data of loess and shale samples are from Beard et al. (2003)

[c] K isotope data are from this study

and high purity D_2 (flow rate: 6 mL/min) as the reaction gas. Argon hydride (ArH^+), the most outstanding issue for high precision $^{41}K/^{39}K$ ratio measurement using MC-ICP-MS, was near quantitatively suppressed via proton transfer and atom transfer reactions with D_2 in the collision cell (Li et al. 2016). Potassium solutions were introduced into the plasma using a self-aspirating Glass Expansion Micromist nebulizer with an uptake rate of $\sim$ 0.1 mL/min and a Glass Expansion Cyclonic spray chamber cooled to 5 °C using a water jacket. Typical sensitivity for 1 ppm K solution under standard mass resolution ($\sim$ 400 resolving power) was 7–11 V on ^{39}K and 0.6–1 V on ^{41}K. It should be noted that in the analytical session for most of samples reported in this study, weak interferences on ^{41}K and ^{39}K were identified during mass scan of blank acid. The mass of these interferences were 0.06–0.08 atomic mass units (AMU) heavier than ^{39}K and ^{41}K, respectively. These interferences cannot be removed using collision cell, therefore the defining slit for the ion beam was narrowed down to about 25% transmission ($>$ 1000 resolving power), to fully resolve these interferences from K isotopes in the mass spectrum. Subsequently, instrument sensitivity was reduced to 1.5–2 V on ^{39}K.

A standard-sample-standard bracketing routine was applied for K isotope ratio measurement, against a 1 ppm or 5 ppm in-house K stock solution (UW-K), depending on if the defining slit was narrowed to avoid isobars. Sample solutions were diluted to match the concentration of standard solution to better than $\pm$ 10%. A 60 s on-peak acid blank was measured prior to each isotopic analysis of K solution, and was subtracted from the analyte signal. Each K isotopic analysis consisted forty 5 s integrations.

2.3 Data reporting, precision, and accuracy

Potassium isotope compositions are reported using the standard per mil (‰) notation of $\delta^{41}K$ for a $^{41}K/^{39}K$ ratio, where $\delta^{41}K = [(^{41}K/^{39}K_{sample})/(^{41}K/^{39}K_{standard}) - 1] \times 1000$. All K isotope data are reported relative to international K standard NIST SRM 3141a. The in-house K stock solution (UW-K) has a $\delta^{41}K$ value of $- 0.12 \pm 0.03$ ‰ (2 standard error, or 2SE, n = 43) relative to NIST SRM 3141a. Internal precision for $^{41}K/^{39}K$ ratio measurement of the method was better than ± 0.07 ‰ (2SE), mostly better than ± 0.04 ‰ (2SE). Accuracy of the method was checked by analyzing pure NIST 3141a K and synthetic samples that were treated as samples using the two-stage ion exchange columns. The synthetic samples were made by mixing UW-K solution with matrix elements separated from different natural samples during ion exchange column chemistry. The measured $\delta^{41}K$ values for five processed NIST 3141a K cluster around 0 ‰ ($- 0.03 \pm 0.13$ ‰, 2SD, n = 5), and the measured $\delta^{41}K$ values for seven synthetic samples that were doped with UW-

K cluster around $- 0.12$ ‰ ($- 0.10 \pm 0.08$ ‰, 2SD, n = 7) (Li et al. 2016). Narrowing of defining slit of MC-ICP-MS did not affect accuracy of K isotope analysis, as the measured seawater $\delta^{41}K$ value using narrow slit and 5 ppm solution was 0.04 ± 0.01 ‰ (2SD, n = 2), which is consistent with $\delta^{41}K$ value of 0.06 ± 0.10 ‰ (2SD, n = 3) reported in Li et al. (2016) that used a standard slit and 1 ppm K solution.

3 Results

The measured K isotope compositions for the shale and loess samples are plotted in Fig. 1 and tabulated in Table 1. Overall there is a 0.6 ‰ variability in $\delta^{41}K$ values within sedimentary samples. The $\delta^{41}K$ values of six loess samples
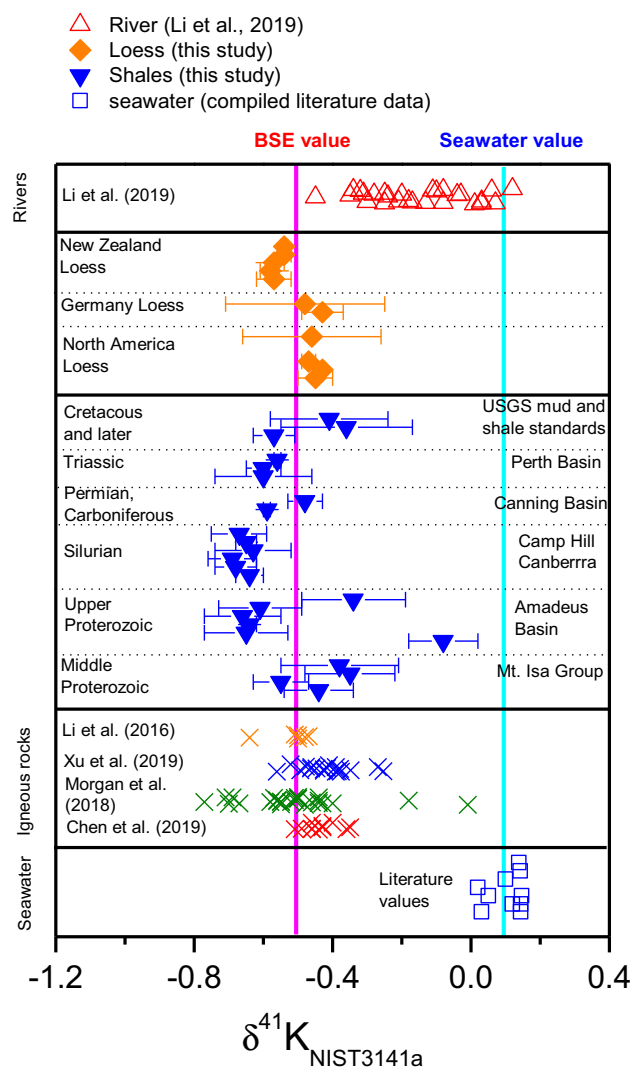
Fig. 1 Comparison of K isotope compositions for rivers, igneous rocks, shales, mud, and loess samples. K isotope data are reported against NIST SRM 3141a. The two vertical colored lines denote baseline values for BSE and seawater, respectively

from North America and Western Europe vary between − 0.48 and − 0.43 ‰, whereas $\delta^{41}K$ values of five loess from New Zealand are slightly more negative and vary between − 0.58 and − 0.54 ‰. Two USGS standards, the Cretaceous Cody Shale (SCo-1) and modern marine mud (MAG-1), have $\delta^{41}K$ values of − 0.41 ‰ and − 0.57 ‰ respectively (Fig. 1, Table 1). The twenty-three post-Archean Australian shales that have been analyzed have $\delta^{41}K$ values that vary from − 0.69 to − 0.08 ‰. The 9 samples from the Mt Isa Group shale and the Canning and Perth basins all have $\delta^{41}K$ that are within 0.15 ‰ of igneous rocks. In contrast the State Circle Shale and Amadeus Basin shale samples have $\delta^{41}K$ values that are typically more than 0.15 ‰ different than igneous rocks. The Silurian State Circle shales all have lower $\delta^{41}K$ values that range from − 0.69 to − 0.63 ‰. Four shale samples from the Amadeus Basin have that range from − 0.61 to − 0.65 ‰ and two other samples have anomalously high $\delta^{41}K$ values of − 0.34 and − 0.08 ‰ (Fig. 1, Table 1).

4 Discussions

4.1 K isotope baseline of the upper continental crust

The K isotope composition for the Bulk Silicate Earth value was first proposed by Wang and Jacobsen (2016), based on analyses of basalts from different localities and tectonic settings. However, subsequent studies have revealed that considerable K isotope variability exist in upper continental rocks, particularly in the evolved, felsic rocks (Chen et al. 2019; Morgan et al. 2018; Xu et al. 2019). For the purpose of understanding global K cycling, it is necessary to estimate the average K isotope composition of upper continental crust, which is an important source of K in seawater. Loess is derived from physical abrasion in a cold climate of typically upper continental crustal material coupled with Aeolian deposition (Taylor et al. 1983), therefore the amount of chemical weathering these sediments have experienced would be limited. Indeed, cross plots of K content versus contents of immobile elements Al and Ti (Fig. 2a, b) show that the loess samples did not experience unequivocal K addition or loss, therefore the possible K isotope fractionation associated with loess formation would be insignificant, and it is possible to infer the average K isotope composition of upper continental crust from loess. The loess samples analyzed in this study have relative uniform K isotope compositions that cluster around − 0.5 ‰, close to the Bulk Silicate Earth value (− 0.48 ‰) proposed by Wang and Jacobsen (2016) (Fig. 1; Table 1). Such consistency implies that, K was enriched in crust during Earth's differentiation without a distinguishable overall K isotope

fractionation between mantle rocks and melts. Further, although seawater is an important geological reservoir and has a K isotope composition distinct from the igneous rocks (Li et al. 2016; Wang and Jacobsen 2016), the mass of K in seawater ($\sim 5.6 \times 10^{20}$ g) is too small compared to that in Earth's continental crust ($\sim 3.5 \times 10^{23}$ g) to shift the isotopic mass balance to a significant degree. Based on the measured K isotope compositions of loess, a $\delta^{41}K$ value of − 0.5 ± 0.1 ‰ is proposed as the $\delta^{41}K$ baseline for average continental crust, the source material of shales that are discussed below.

4.2 K isotope fractionation recorded in shales

In contrast to the limited K isotope variability in loess, the K isotope composition of shales varies over a 0.6 ‰ range in $\delta^{41}K$ values (Fig. 1; Table 1). This range in K isotope compositions is correlated to K addition for many samples. For example, cross plots of K content versus immobile element concentration of Al and Ti show that the majority of shale samples have experienced K addition by over 50% of the original contents (Fig. 2a, b). Because the particulate precursor of shales is depleted in K (Amundson 2004; Viers et al. 2009), a K enrichment process must have occurred in sedimentary basins during and after deposition, through interaction between the shale precursor with seawater and pore fluids in the sediment. A large proportion of the shales display a negative correlation between $\delta^{41}K$ values and K_2O concentration (Fig. 2d), that is interpreted to reflect addition or incorporation of K with a low $^{41}K/^{39}K$ ratio during deposition and post-depositional processes. Enrichment of K is mirrored by Na depletion in shales (Fig. 2c), and the $\delta^{41}K$ values of a large proportion of the shales decrease with increasing K/Na ratios (Fig. 2e). These facts suggest that the K isotope fractionation process may be accompanied by either K–Na exchange in existing clay minerals, or neoformation of K-rich minerals (e.g., illite) at the expense of dissolution of Na-silicates (e.g., albite).

In the cross plots of $\delta^{41}K$ versus K, K/Na and K/Al (Fig. 2d, e), a few samples do not follow the negatively-correlated trend defined by the majority of the shales. Iron isotopes provide hints about the origin of shale with elevated $\delta^{41}K$ values. The shale sample (A012 of Amadeous Basin Shale, Table 1) with the highest $\delta^{41}K$ value has the highest $\delta^{56}Fe$ value among the shales (Fig. 2f), and another the Amadeous Basin Shale sample with a more typical shale K isotope compositions has one of the lowest $\delta^{56}Fe$ value (− 0.28 ‰, sample AO07, Table 1) of the shales analyzed by Beard et al. (2003). Thus, the Amadeous Basin shales define a 0.6 ‰ range in Fe isotope compositions which stands in marked contrast to the Fe isotope variation (0 ± 0.1 ‰ in $\delta^{56}Fe$) found in modern marine sediments,
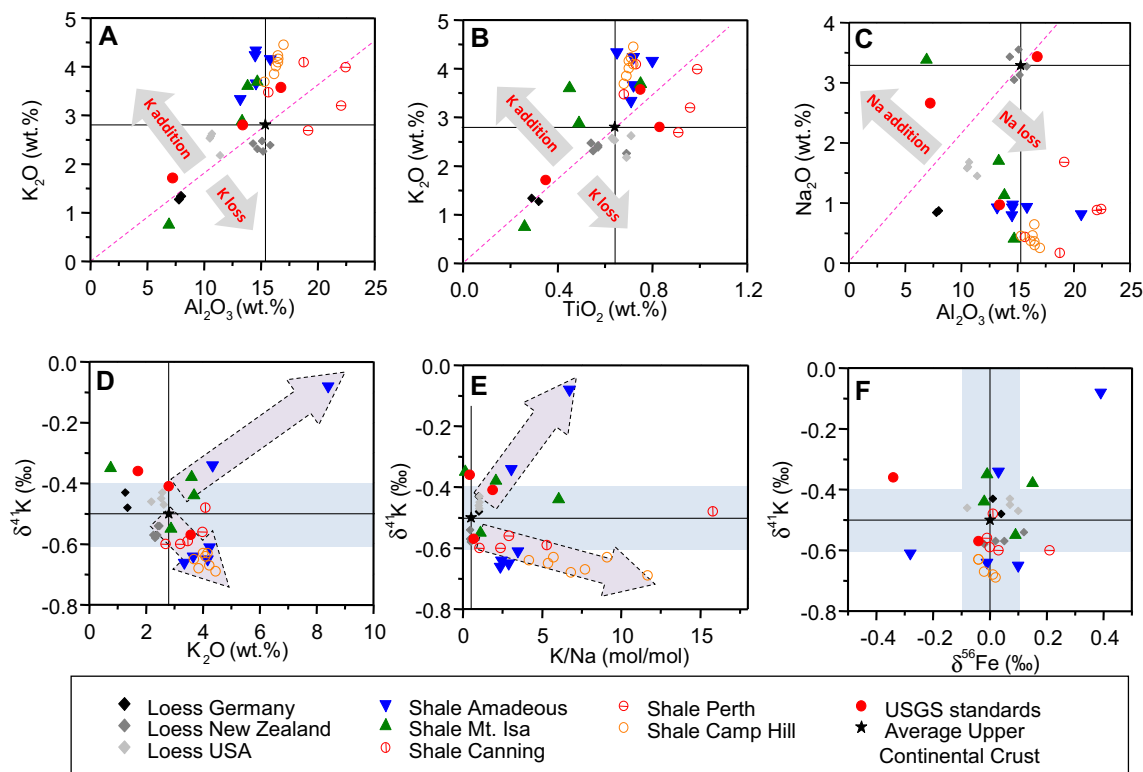
Fig. 2 Cross plots of **a** Al_2O_3 vs K_2O, **b** TiO_2 vs K_2O, **c** Al_2O_3 vs Na_2O, **d** $\delta^{41}K$ vs K_2O, **e** $\delta^{41}K$ vs K/Na and **f** $\delta^{41}K$ vs $\delta^{56}Fe$ for the loess and shale samples. A sample with very high K_2O (8.41 wt%) content was not plotted in plots A and B for clarity. The elemental concentrations for average upper continental crust are from Rudnick and Gao (2003) and marked with filled star and horizontal and vertical lines. The pink dashed line that goes through the point of origin and the point of continental crust delineates the fields of elemental gain or loss for loess and shales. The $\delta^{41}K$ of average upper continental crust is set at 0.5 ± 0.1 ‰. The analytical errors for the samples scatter about ± 0.1 ‰. The arrows in the plots are discussed in the text

river suspended materials, loess and aerosols (Beard et al. 2003). Because solubility of Fe(III) phases in oxidized aqueous conditions is extremely low (Kuma et al. 1996) and large Fe isotope fractionation is ubiquitously associated with redox processes of Fe (Johnson et al. 2008), the Fe isotope variation in Amadeous Basin Shales was likely produced via post-depositional processes in the sediments, where redox-driven Fe cycling and Fe isotope fractionation was feasible. The elevated $\delta^{41}K$ signatures in shales may have been produced via post-depositional processes such as glauconite production. Glauconite is a K rich mica with some reduced Fe (Meunier and El Albani 2007) and production of this mineral may have changed both the Fe and K isotope composition or the sample.

4.3 K isotope response to global K cycling

Because significant K isotope fractionation occurs during silicate weathering and clay formation (Li et al. 2019), stable K isotopes offer a novel approach to quantify the relative contributions of continental weathering and mid-ocean ridge activities for the K global cycle, based on a few assumptions of chemical and isotopic steady state of

seawater. As suggested in Li et al. (2019), elemental and isotopic mass balance for K in oceans can be formularized as:

$$J_{riv} + J_{MOR} = J_{clay} + J_{alt} \tag{1}$$

$$\delta_{riv}J_{riv} + \delta_{MOR}J_{MOR} = \delta_{clay}J_{clay} + \delta_{alt}J_{alt} \tag{2}$$

where J and δ represent the K flux and K isotope compositions for riverine inputs ($_{riv}$), K released from high temperature mid-ocean hydrothermal fluids ($_{MOR}$), as well as K incorporated into clay minerals in sediments ($_{clay}$), and K removed through low temperature alteration of basalts ($_{alt}$), respectively. Combining Eqs. (1) and (2), we can derive:

$$\delta_{clay} = \left[\frac{J_{riv}}{J_{MOR}} \cdot \delta_{riv} + \delta_{MOR} + \frac{J_{alt}}{J_{MOR}} \cdot (\delta_{clay} - \delta_{alt}) \right] \Bigg/ \left[\frac{J_{riv}}{J_{MOR}} + 1 \right] \tag{3}$$

Equation (3) shows that K isotope composition of clay is essentially a function of J_{riv}/J_{MOR}. The other parameters in the equation can be obtained from Eqs. (1) and (2) based on modern K cycling. There have been significant uncertainties in the literature data for estimated J_{riv} (Berner and

Berner 2012; Holland 2005; Jarrard 2003), J_{MOR} (Holland 2005; Jarrard 2003), J_{clay} (Bloch and Bischoff 1979; Holland 2005; Jarrard 2003), and J_{alt} (Bloch and Bischoff 1979; Elderfield and Schultz 1996b; Holland 2005; Jarrard 2003; Staudigel 2014), more recently the large uncertainties in J_{MOR} and J_{clay} have been remarkably reduced by Monte Carlo simulations (Li et al. 2019), and based on the average values of the Monte Carlo simulation results in Li et al. (2019), we set $J_{riv} = 5.5 \times 10^{13}$ g y^{-1}, $J_{MOR} = 0.8 \times 10^{13}$ g y^{-1}, $J_{clay} = 4.9 \times 10^{13}$ g y^{-1}, and $J_{alt} = 1.4 \times 10^{13}$ g y^{-1}. The study of Li et al. (2019) also gave new estimates of $\delta_{riv} = -0.22$ ‰. Based on the study of Parendo et al. (2017), δ_{alt} is set as the modern seawater value (+ 0.1 ‰). δ_{MOR} is set as -0.6 ‰ based on the assumption that little K isotope fractionation occurred at high temperature when hydrothermal fluid leaches K from basalts in MOR center. Using the above parameters and solving Eq. (2), δ_{clay} is calculated to be -0.4 ‰.

Analyzing Eq. (3), we note that the term $\delta_{clay}-\delta_{alt}$ is a constant (-0.5 ‰) that reflects the difference in K isotope fractionation factor between the seawater-clay and seawater-altered basalt pairs. On the other hand, high continental weathering intensity would bring more detrital materials and Al into oceans to boost clay formation, whereas higher MOR activity would enlarge the zone of low temperature seawater-basalt interaction. Therefore, we assume that J_{MOR}/J_{Riv} is positively correlated with J_{Alt}/J_{clay} at variable conditions:

$$J_{MOR}/J_{Riv} = q \times J_{alt}/J_{clay} \quad (4)$$

q is set as a constant, and using the modern flux data, q is calculated to be 0.5, subsequently, J_{alt}/J_{MOR} in Eq. (3) can be calculated based on this function and Eq. (1) in the discussion. Using Eqs. (3) and (4), and the parameters defined above, we can model the relation between K isotope composition of clays and the relative contribution of MOR fluids for the K influx to ocean (Fig. 3). Assuming a $\Delta^{41}K_{sw-clay}$ fractionation of 0.5 ‰ between seawater and clays, the curve for seawater is also derived. We note that there are uncertainties in the parameters in Eqs. (3) and (4) that may lead to inaccuracy in modeling results. However, changes in these parameters shift the curves up and down and along the y axis but they do not change the trend and pattern of the curves. Figure 3 shows that in a scenario of little continental weathering, but dominant MOR activity, which likely occurred in early Earth and the Snowball Earth period, $\delta^{41}K$ of seawater is essentially buffered by igneous rocks at high temperature and should be down to -0.6 ‰. In contrast, in a scenario of dominant continental weathering but very weak MOR activity, $\delta^{41}K$ of clays should be close to $\delta^{41}K$ of riverine input and the $\delta^{41}K$ of seawater should be 0.5 ‰ higher. Phanerozoic shales analyzed in this study cover a range of -0.7 to -0.4 ‰
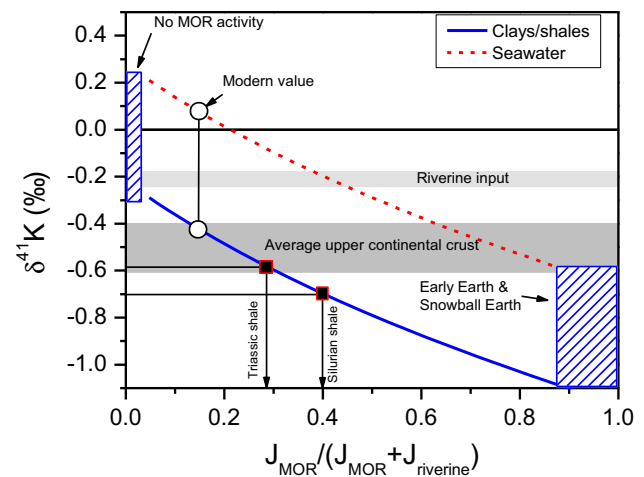
Fig. 3 Modeled K isotope composition of clays and seawater as a function of the ratio of MOR-sourced K flux to total K influx into oceans, based on a K isotope mass balance model. Filled squares represent the measured data from Australian shales

in $\delta^{41}K$, and the increase in $\delta^{41}K$ from -0.7 ‰ for Silurian shales to -0.6 ‰ for Triassic shales corresponds to a ca. 10% decrease of MOR fluids contribution to the total K influx (Fig. 3). This is consistent with the study of Hardie (1996), who calculated that the ratio between riverine input and MOR input increased by a factor of 20% from Silurian to Triassic.

5 Conclusions and implications

Significant K isotope variability has been observed in shales, and the majority of the shales follow a trend of decreasing $\delta^{41}K$ with increasing K content, implying preferential uptake of light K isotopes into clay minerals in oceanic sediments. Global cycling of K involves continental weathering, clay formation in oceanic sediments, and hydrothermal alteration of seafloor basalts. These processes are associated with K isotope fractionation, thus K isotopes could be used to understand global K cycling. Fluxes of K in oceans involving continental weathering and mid-ocean ridge hydrothermal activities may have changed in geological histories in response to secular climate change or plate tectonics, and these may result in change in $\delta^{41}K$ of seawater. It is possible that the changes in $\delta^{41}K$ of seawater may be recorded in shales, and K isotope compositions of shales may hold clues for understanding the major events (e.g., melting of Snowball Earth) of global K cycling in geological history.

References

Amundson R (2004) Soil formation. In: Holland HD, Turekian KK (eds) Treatise on geochemistry, vol 5. Elsevier, Amsterdam, pp 1–35

Beard BL, Johnson CM, Von Damm KL, Poulson RL (2003) Iron isotope constraints on Fe cycling and mass balance in oxygenated Earth oceans. Geology 31:629–632

Berner EK, Berner RA (2012) Global environment: water, air, and geochemical cycles. Princeton University Press, Princeton

Berner RA, Lasaga AC, Garrels RM (1983) The carbonate-silicate geochemical cycle and its effect on atmospheric carbon dioxide over the past 100 million years. Am J Sci 283:641–683

Bloch S, Bischoff JL (1979) The effect of low-temperature alteration of basalt on the oceanic budget of potassium. Geology 7:193–196

Chen H, Tian Z, Tuller-Ross B, Korotev Randy L, Wang K (2019) High-precision potassium isotopic analysis by MC-ICP-MS: an inter-laboratory comparison and refined K atomic weight. J Anal At Spectrom 34:160–171

Elderfield H, Schultz A (1996a) Mid-ocean ridge hydrothermal fluxes and the chemical composition of the ocean. Annu Rev Earth Planet Sci 24:191–224

Elderfield H, Schultz A (1996b) Mid-ocean ridge hydrothermal fluxes and the chemical composition of the ocean. Annu Rev Earth Planet Sci 24:191–224

Flanagan FJ (1976) Descriptions and analyses of eight new USGS rock standards. U.S. Geological Survey Professional Paper 840, pp 1–192

Garrels RM, Mackenzie FT (1971) Evolution of sedimentary rocks. Norton, New York

Hardie LA (1996) Secular variation in seawater chemistry: an explanation for the coupled secular variation in the mineralogies of marine limestones and potash evaporites over the past 600 m.y. Geology 24:279–283

Holland HD (2005) Sea level, sediments and the composition of seawater. Am J Sci 305:220–239

Hu Y, Chen X-Y, Xu Y-K, Teng F-Z (2018) High-precision analysis of potassium isotopes by HR-MC-ICPMS. Chem Geol 1:1. https://doi.org/10.1016/j.chemgeo.2018.05.033

Humayun M, Clayton RN (1995) Precise determination of the isotopic composition of potassium: application to terrestrial rocks and lunar soils. Geochim Cosmochim Acta 59:2115–2130

Jarrard RD (2003) Subduction fluxes of water, carbon dioxide, chlorine, and potassium. Geochem Geophys Geosyst. https://doi.org/10.1029/2002GC000392

Johnson CM, Beard BL, Roden EE (2008) The iron isotope fingerprints of redox and biogeochemical cycling in modern and ancient earth. Annu Rev Earth Planet Sci 36:457–493

Kronberg BI (1985) Weathering dynamics and geosphere mixing with reference to the potassium cycle. Phys Earth Planet Interiors 41:125–132

Kuma K, Nishioka J, Matsunaga K (1996) Controls on iron(III) hydroxide solubility in seawater: the influence of pH and natural organic chelators. Limnol Oceanogr 41:396–407

Li W (2017) Vital effects of K isotope fractionation in organisms: observations and a hypothesis. Acta Geochim 36:374–378

Li S, Li, W, Beard BL, Raymo ME, Wang X, Chen Y, Chen J (2019) K isotopes as a tracer for continental weathering and geological K cycling. In: Proceedings of the national academy of sciences, p 201811282

Li W, Beard BL, Li S (2016) Precise measurement of stable potassium isotope ratios using a single focusing collision cell multi-collector ICP-MS. J Anal At Spectrom 31:1023–1029

Li W, Kwon KD, Li S, Beard BL (2017) Potassium isotope fractionation between K-salts and saturated aqueous solutions at room temperature: laboratory experiments and theoretical calculations. Geochim Cosmochim Acta 214:1–13

Meunier A, El Albani A (2007) The glauconite–Fe-illite–Fe-smectite problem: a critical review. Terra Nova 19:95–104

Meybeck M (2003) Global occurrence of major elements in rivers. In: Drever JI (ed) Treatise on geochemistry. Elsevier, Amsterdam, pp 207–223

Morgan LE, Ramos DPS, Davidheiser-Kroll B, Faithfull J, Lloyd NS, Ellam RM, Higgins JA (2018) High-precision 41 K/39 K measurements by MC-ICP-MS indicate terrestrial variability of δ 41K. J Anal At Spectrom 33:175–186

Nance WB, Taylor SR (1976) Rare earth element patterns and crustal evolution-I. Australian post-Archean sedimentary rocks. Geochim Cosmochim Acta 40:1539–1551

Parendo CA, Jacobsen SB, Wang K (2017) K isotopes as a tracer of seafloor hydrothermal alteration. Proc Natl Acad Sci 114:1827–1831

Palme H, O'Neill HSC (2014) Cosmochemical estimates of mantle composition. In: Treatise on geochemistry, 2nd edn. Elsevier, Oxford, pp 1–39

Raymo ME, Ruddiman WF (1992) Tectonic forcing of late Cenozoic climate. Nature 359:117

Rudnick RL, Gao S (2003) Composition of the continental crust. In: Holland HD, Turekian KK (eds) Treatise on geochemistry. Elsevier, Amsterdam, pp 1–64

Staudigel H (2014) Chemical fluxes from hydrothermal alteration of the oceanic crust. In: Holland HD, Turekian KK (eds) Treatise on geochemistry, 2nd edn. Elsevier, London, pp 583–606

Taylor SR, McLennan SM, McCulloch MT (1983) Geochemistry of loess, continental crustal composition and crustal model ages. Geochim Cosmochim Acta 47:1897–1905

Viers J, Dupre B, Gaillardet J (2009) Chemical composition of suspended sediments in World Rivers: new insights from a new database. Sci Tot Environ 407:853–868

Wang K, Jacobsen SB (2016) An estimate of the Bulk Silicate Earth potassium isotopic composition based on MC-ICPMS measurements of basalts. Geochim Cosmochim Acta 178:223–232

Xu Y-K, Hu Y, Chen X-Y, Huang T-Y, Sletten RS, Zhu D, Teng F-Z (2019) Potassium isotopic compositions of international geological reference materials. Chem Geol 513:101–107